



Characterization of light-induced potentials in the strong-field dissociation of O_2^+

P. M. Abanador and U. Thumm *

J. R. Macdonald Laboratory, Department of Physics, Kansas State University, Manhattan, Kansas 66506, USA

 (Received 11 September 2020; accepted 10 November 2020; published 24 November 2020)

We investigate theoretically the imprints of light-induced potentials (LIPs) on the dissociation dynamics of O_2^+ molecular ions, as observable in angle-resolved fragment kinetic-energy-release (KER) spectra. Following the vibrational and rotational dynamics of the initial pump-laser-excited cationic nuclear wave packet, while accounting for the dipole coupling between the $O_2^+(a^4\Pi_u)$ and $O_2^+(f^4\Pi_g)$ electronic states in 800-nm 40-fs probe-laser pulses with peak intensities between 10^{13} and 10^{14} W/cm², we calculate angle-resolved KER spectra which reveal characteristic energy- and angle-dependent fringe structures. These fringes shift downward in energy as the molecular alignment angle θ relative to the probe-pulse polarization direction increases from 0 to $\pi/2$. The angle-dependent shifts in the KER fringes increase for larger probe-pulse peak intensities and follow the angle and light-wave-intensity dependence of the vibrational spectrum in the associated Floquet bond-hardening well, which is a manifestation of transient O_2^+ nuclear-probability trapping in the LIP during dissociation. By examining the rovibrational dynamics of the dissociating molecular cation near the light-induced conical intersection (LICI) in the cationic LIP surface at $\theta = \pi/2$, we identify related angle-dependent structures in the KER spectra, suggesting a means for assessing the significance of LICIs in molecular dissociation pathways.

DOI: [10.1103/PhysRevA.102.053114](https://doi.org/10.1103/PhysRevA.102.053114)

I. INTRODUCTION

The dissociation of molecules by intense, short laser pulses is a fundamental physical light-matter-interaction process. In many cases, notably for diatomic molecules, the dissociation dynamics can be resolved in time by repeatedly exciting (and possibly ionizing) molecules in ultrashort pump-laser pulses and destructively imaging the excited nuclear dynamics with delayed ultrashort probe-laser pulses for a series of delays between the pump- and probe-laser pulses (see, e.g., [1–3] and references therein). A prototypical and the most elementary example is given by the femtosecond time-resolved imaging of the bound and dissociative nuclear dynamics in H_2^+ (or D_2^+) molecular ions in pump-probe experiments by measuring and analyzing fragment kinetic-energy-release (KER) spectra [4–6]. In this pump-probe scheme, for appropriate pulse intensities, the ionization of the neutral parent molecule H_2 in the pump pulse launches a nuclear wave packet in the electronic ground state of H_2^+ . The electric field of a second, delayed probe-pulse dipole couples the binding $H_2^+(1\sigma_g)$ cationic ground state to the repulsive $H_2^+(2p\sigma_u)$ state (or higher repulsive states), allowing for the dissociation into a proton and an (excited) hydrogen atom and thus the recording of the fragments' asymptotic kinetic energy for different pump-probe delays.

The initial nuclear wave packet created by the ultrashort pump pulse is frequently approximated by assuming the instantaneous ionization of the parent molecule within the Franck-Condon (FC) approximation, i.e., by modeling the initial cationic vibrational-state distribution in terms of the

wave-function overlap of the parent molecule's vibrational ground state with vibrational states in the $H_2^+(1\sigma_g)$ state [7,8]. The phases of the vibrational-state constituents of the initial H_2^+ nuclear wave packet remain undetermined and are usually (arbitrarily) set equal to zero. Once the initial H_2^+ nuclear wave packet is determined, its evolution, subject to a linearly polarized infrared (IR) probe pulse, can be calculated by numerically solving the time-dependent Schrödinger equation (TDSE) on a set of relevant Born-Oppenheimer (BO) potential energy curves. Such nuclear wave-function-propagation calculations are conveniently performed in one dimension, the internuclear distance R , thereby solely taking into account the molecular ion's vibrational dynamics while assuming the molecular axis remains fixed in space [1,9,10]. Nuclear wave-function-propagation calculations for H_2^+ have been extended to model the coupled rotational and vibrational nuclear motion by solving the TDSE in two dimensions, R and the molecular alignment angle θ relative to the laser-polarization direction [3,11–13]. For the dissociation of diatomic molecules, two-dimensional TDSE calculations remain computationally as well as conceptually tractable and therefore allow for a detailed study of the rovibrational light-induced dynamics during the dissociation process. Despite their comparatively simple structure, the dissociative ionization of hydrogen molecules has been addressed in numerous pump-probe investigations that impressively revealed quantum-mechanical phenomena such as nuclear wave-packet revivals [5,8,14], charge-resonance enhanced ionization [15–17], and bond softening and bond hardening [8,18–21].

While the same phenomena are expected to be present in heavier diatomic molecules, understanding the light-induced nuclear dynamics is significantly more demanding than for

*thumm@phys.ksu.edu

hydrogen molecules, due to their more complex electronic structure. In general, for heavier diatomic molecules, the pump pulse generates coherent nuclear wave packets that simultaneously evolve on different potential energy surfaces, where they are candidates for dipole coupling in the probe- (and possibly also pump-) laser electric field to a variety of adiabatic molecular electronic states. Nevertheless, nuclear excitation and dissociation pathways have recently been distinguished in experimental and theoretical studies on N_2 [22,23], O_2 [1–3,10,22–24], CO [22,23], and noble-gas dimers [25,26] for IR-IR [10,22,23,25,26], extreme ultraviolet (XUV)-IR [1,2], XUV-XUV [24], and IR-soft-x-ray [27] pump-probe-pulse combinations. For O_2 , in particular, the experiment performed by De *et al.* [23] with intense few-cycle 800-nm pump- and probe-laser pulses revealed pronounced oscillations of the O^+ fragment yield as a function of the fragment kinetic energy at KER values below 0.5 eV. The sequence of observed low-KER peaks overlaps with the vibrational spectrum of the first excited cationic state $O_2^+(a^4\Pi_u)$, suggesting dissociation into the $O^+ + O$ breakup channel to be initiated by the pump pulse launching a nuclear wave packet in the $O_2^+(a^4\Pi_u)$ state. This nuclear wave packet subsequently expands to larger internuclear distances via its transition to the dissociative $O_2^+(f^4\Pi_g)$ state by absorption of a single probe-pulse photon.

The dominant role of the $a^4\Pi_u$ and $f^4\Pi_g$ adiabatic electronic states of O_2^+ in $O_2 \rightarrow O^+ + O$ dissociation was confirmed in the XUV-pump-IR-probe experiment and accompanying theoretical modeling of Cörlin *et al.* [1]. From the analysis of O^+ KER spectra, this study tracked the transient nuclear motion in O_2^+ in both the time and frequency domains. Specifically, the $O_2^+(a^4\Pi_u)$ and $f^4\Pi_g$ adiabatic states were identified with (i) nuclear wave-packet oscillations and revivals in pump-probe-delay-dependent KER spectra and (ii) quantum-beat structures in the associated Fourier-transformed (power) spectra. A prevalence of the $O_2^+(a^4\Pi_u)$ and $f^4\Pi_g$ states was also observed in the recent O_2 XUV-pump-IR-probe dissociative ionization experiment of Malakar *et al.* [2] by examining contributions to the measured O^+ yields from one-, two-, and three-photon-dissociation pathways. A recent theoretical study by Xue *et al.* [10] reexamined these previous investigations of O_2 dissociative ionization, modeling the nuclear motion in the molecular cation within a three-state close-coupling calculation that includes the $O_2^+(b^4\Sigma_g)$ excited state, in addition to the $a^4\Pi_u$ and $f^4\Pi_g$ BO states. The authors found that, while the molecular-alignment-dependent dipole coupling of the $b^4\Sigma_g$ and $a^4\Pi_u$ states can lead to noticeable population transfer to the $b^4\Sigma_g$ state and account for minor changes in KER spectra, the inclusion of the $b^4\Sigma_g$ state only slightly improves the agreement with experimental KER spectra, as compared with Ref. [23]. Overall, the experimental data in Refs. [1,23] do not provide clear evidence for the participation of the $b^4\Sigma_g$ state as an intermediate channel in the dissociation process. This conclusion remains valid for the recent experiment of Malakar *et al.* [2].

Underlying the discussed identification of dissociation pathways are light-induced potentials (LIPs) [19–21,28–30]. These LIPs are provided within Floquet theory as the result of coupling molecular BO states in the presence of a laser field, including any number of allowed light-induced

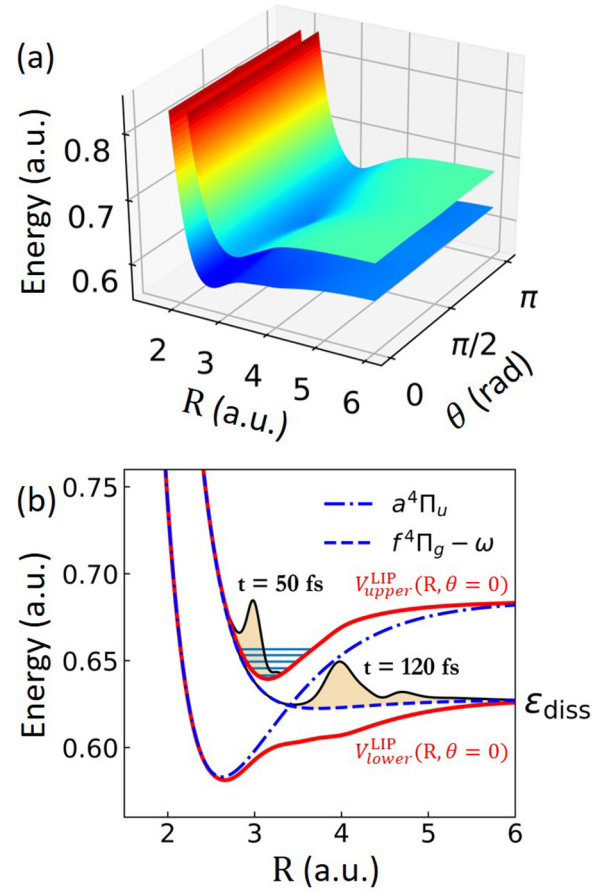


FIG. 1. Light-induced Floquet potentials V_{lower}^{LIP} and V_{upper}^{LIP} for the two-channel model of the O_2^+ molecular ion in an external field with a wavelength of 800 nm and a peak intensity of 10^{14} W/cm 2 . (a) Field-dressed potential energy surfaces as a function of the internuclear distance R and the molecular alignment angle θ . (b) Corresponding field-dressed Floquet curves along the aligned direction $\theta = 0$ (red solid curve) and field-free BO potential energy curves for the $O_2^+(a^4\Pi_u)$ (blue dash-dotted curve) and $O_2^+(f^4\Pi_g)$ (blue dashed curve) states. The five lowest vibrational levels ($v = 0 - 4$) in $V_{upper}^{LIP}(R, \theta = 0)$ are indicated by turquoise horizontal lines. Two snapshots of the nuclear motion along the $\theta = 0$ direction are shown in terms of the nuclear probability density in the upper state $\rho_2(t)$ at the peak of the laser pulse ($t = 50$ fs after the wave packet was launched) and after the pulse has passed (at $t = 120$ fs).

dipole transitions [31,32]. Even though *conventional* Floquet theory assumes continuous-wave light fields, the Floquet picture has been widely and successfully implemented to understand molecular dissociation in pulsed light fields. As an example, Fig. 1(a) shows the LIPs obtained from the dipole coupling of the field-free BO $a^4\Pi_u$ and $f^4\Pi_g$ states of O_2^+ in an 800-nm light field with an intensity of $I_0 = 10^{14}$ W/cm 2 . The calculated LIPs include a light-induced conical intersection (LICI) [33–35] at $\theta = \pi/2$ and $R_{1\omega} \approx 3.4$ a.u., where the lower Floquet LIP V_{lower}^{LIP} and the upper Floquet LIP V_{upper}^{LIP} become degenerate. Throughout this work, we use atomic units (a.u.), unless specified otherwise. The corresponding Floquet curves, obtained as cuts through the LIP surfaces at $\theta = 0$, i.e., for molecules that are aligned with the polarization direction of the linearly polarized probe laser, are shown in Fig. 1(b) as

red solid curves, together with the field-free $O_2^+(a^4\Pi_u)$ and $f^4\Pi_g$ BO potential curves (dash-dotted and dashed curves). This graph illustrates the formation of vibrational states in the bond-hardening well of $V_{\text{upper}}^{\text{LIP}}$. While pump-probe experiments employ very short pulses, bond-hardening wells in the LIPs, which arise transiently during a molecule's exposure to an intense laser pulse, have long been discussed as promoting molecular stabilization, i.e., decreasing dissociation yields for increasing laser intensity [31,36,37].

In the present work we examine the effects of transient nuclear probability trapping and LICIs on the dissociation dynamics of O_2^+ molecular ions during $O_2 \rightarrow O^+ + O$ dissociation, following up on our previous demonstration of molecular-bond hardening during the dissociation of O_2^+ by intense probe pulses with durations between 10 and 50 fs [3]. We note that in this scenario the probe pulse serves two purposes, as it not only steers the nuclear dynamics in O_2^+ , but also allows the destructive imaging of the molecular cation's nuclear motion by analysis of the fragment-momentum distribution. In Sec. II we review the applied theoretical methods, by first summarizing our numerical approach for solving the TDSE in one (R) or two (R and θ) nuclear degrees of freedom in Sec. II A and then commenting in Sec. II B on our use of Floquet theory for analyzing our numerical results. In Sec. III we discuss distinct structures in the angle-resolved KER spectra resulting from our TDSE calculations as signatures of transient nuclear-probability-density confinement (bond hardening) (Sec. III A) and the rovibrational nuclear dynamics near the LICI (Sec. III B). We conclude with a brief summary in Sec. IV.

II. THEORETICAL METHODS

A. TDSE calculations

Modeling the launching of a nuclear wave packet from the ground state of the neutral O_2 molecule into the $O_2^+(a^4\Pi_u)$ adiabatic electronic state by an ultrashort intense pump pulse within the FC approximation [7,8], we investigate the subsequent rovibrational nuclear dynamics of the excited molecular cation subjected to a linearly polarized IR-probe field. Within the BO approximation, we numerically solve the TDSE restricted to the two relevant electronic states, $O_2^+(a^4\Pi_u)$ and $O_2^+(f^4\Pi_g)$ [1,2,9,10]. We assume the initial O_2^+ wave packet to be rotationally cold at 0 K, i.e., in the rotational ground state with rotational quantum number $J = 0$ and an isotropic alignment distribution. With these restrictions, the TDSE for the nuclear motion in O_2^+ translates to the set of coupled equations

$$i \frac{\partial}{\partial t} \begin{pmatrix} \psi_1(t) \\ \psi_2(t) \end{pmatrix} = \hat{H}(t) \begin{pmatrix} \psi_1(t) \\ \psi_2(t) \end{pmatrix}, \quad (1)$$

with the Hamiltonian

$$\hat{H}(t) = \begin{pmatrix} T_{\text{nuc}} + V_1(R) & d_{12}(R)E(t) \cos \theta \\ d_{12}(R)E(t) \cos \theta & T_{\text{nuc}} + V_2(R) \end{pmatrix}. \quad (2)$$

We designate the nuclear-wave-packet components that evolve out of the initially occupied $O_2^+(a^4\Pi_u)$ and the initially empty $O_2^+(f^4\Pi_g)$ field-free states as $\psi_1(R, \theta, t)$ and $\psi_2(R, \theta, t)$, respectively. The diagonal elements in the Hamil-

tonian matrix include the field-free potential energy curves $V_i(R)$ corresponding to the BO electronic states $O_2^+(a^4\Pi_u)$ ($i = 1$) and $O_2^+(f^4\Pi_g)$ ($i = 2$).

For the description of the dissociation dynamics in O_2^+ , we consider two alternatives for the numerical solution of the TDSE: (i) treating the alignment angle θ as a fixed parameter, i.e., prohibiting rotational excitations, and (ii) representing R and θ as dynamical variables. Throughout this work, we refer to scheme (i) as one-dimensional (1D) calculation and 1D result(s) and to alternative (ii) as 2D calculation and 2D result(s). The full-dimensional dynamics in both R and θ is incorporated in the 2D calculations, while the rotational motion is frozen in the 1D calculations, where the angular momentum operator L_θ is set to zero in the Hamiltonian (2). Accordingly, we employ the nuclear kinetic energy operators

$$T_{\text{nuc}} = \frac{1}{2\mu} \begin{cases} -\frac{\partial^2}{\partial R^2} + \frac{L_\theta^2}{R^2}, & \text{2D calculation} \\ -\frac{\partial^2}{\partial R^2}, & \text{1D calculation,} \end{cases} \quad (3)$$

with the reduced mass μ . The comparison of numerical results from 1D and 2D calculations provides a way to evaluate the effects of rotational excitation on the nuclear dynamics. In particular, as demonstrated in Sec. III B below, this comparison allows us to distinguish effects on the nuclear dynamics near the LICI that are primarily due to rotational excitations. The off-diagonal elements (2) represent the interaction of the molecular ion with the probe-laser field $E(t)$ in terms of the transition-dipole moment $d_{12}(R)$ between the $a^4\Pi_u$ and $f^4\Pi_g$ states.

For all numerical applications discussed in Sec. III, we consider probe-laser pulses with a fixed wavelength of 800 nm and a \cos^2 electric-field temporal profile with a full width at the amplitude half maximum of 40 fs, corresponding to a spectral bandwidth of 0.08 eV. The center of the probe pulse is chosen to be delayed by $t = 50$ fs, relative to the instant of O_2 ionization by the pump pulse that defines $t = 0$. Within the above-distinguished 1D and 2D calculations, we numerically solve the TDSE by propagating the O_2^+ nuclear wave packet on either a one-dimensional spatial grid (in R) or a two-dimensional spatial grid (in R and θ), respectively. From our TDSE calculations, we obtain angle-resolved KER spectra by Fourier transformation of the dissociative nuclear-wave-function component as a function of R outside the cutoff internuclear distance $R_{\text{cut}} = 6$ a.u., i.e., for $R > R_{\text{cut}}$ [3,9], along individual alignment angles θ . For this final step of the calculation, keeping θ at a constant value amounts to invoking the axial-recoil approximation. We ensure that our numerical results are well converged with respect to all numerical grid parameters, the choice of R_{cut} , and the total propagation time.

B. Floquet analysis

Within the Floquet description, we interpret the field-driven nuclear dynamics in terms of the light-induced potentials $V_{\text{lower}}^{\text{LIP}}(R, \theta)$ and $V_{\text{upper}}^{\text{LIP}}(R, \theta)$ for each component $\psi_i(R, \theta, t)$, $i = 1, 2$, of the nuclear wave packet in Eq. (1). For the intensity $I_0 = 10^{14}$ W/cm², Fig. 1(a) illustrates that the field-induced dipole coupling between the $a^4\Pi_u$ and $f^4\Pi_g$ states of O_2^+ leads to LIPs which vary as a function of the alignment angle θ . Since the transition-dipole moment

between these states is parallel to the molecular axis, the projection of the electric field on the molecular axis amounts to an effective field strength $E_{\text{eff}} = E_0 \cos \theta$, where $E_0 \propto \sqrt{I_0}$ is the peak field strength of the probe pulse. As seen in Fig. 1(b), the corresponding field-dressed (Floquet) curves along the aligned direction $\theta = 0$ indicate an avoided crossing close to the intersection of the field-free $a^4\Pi_u$ potential curve and the field-free $f^4\Pi_g$ potential curve, downshifted by the photon energy ω . The upper Floquet curve features a bond-hardening well, wherein the nuclear wave packet can be transiently trapped during the presence of the probe-pulse electric field. As an example, we show in Fig. 1(b) two snapshots of the nuclear probability density in the upper state, $\rho_2(t) = |\psi_2(R, \theta, t)|^2$, for cations that are aligned with the probe-pulse-polarization direction ($\theta = 0$), obtained from the numerical solution of Eq. (1). At the peak of the laser pulse ($t = 50$ fs), the nuclear wave packet is localized within the bond-hardening well, while after the cations' exposure to the probe pulse, at $t = 120$ fs, a significant part of the nuclear probability dissociates in the O_2^+ ($f^4\Pi_g$) channel.

The Floquet light-induced potentials $V_{\text{lower}}^{\text{LIP}}$ and $V_{\text{upper}}^{\text{LIP}}$ in Fig. 1 are calculated for laser fields with an effective field strength $E_{\text{eff}} = E_0 \cos \theta$ and for fixed molecular alignment angles θ . The associated LIPs also give valuable insight for understanding the dissociation dynamics of O_2^+ in strong *pulsed* few-cycle probe fields with peak electric field strength E_0 . As a measure for the influence of the transient bond-hardening well in $V_{\text{upper}}^{\text{LIP}}$ on the fragment KER, we take as a guide its few lowest vibrational stationary states $\{|v(E_0, \theta)\rangle^{\text{LIP}}\}$ with energies $\{\varepsilon_v^{\text{LIP}}(E_0, \theta)\}$, shown as turquoise horizontal lines in Fig. 1(b). Accepting this guide amounts to an adiabatic picture, i.e., to the assumption of the probe-pulse-induced upper LIP varying slowly on the timescale of the vibrational motion which its bond-hardening well supports.

In order to identify the transient trapping of the O_2^+ wave packet, we compare the dependence on E_0 and θ of the O^+ fragment yield in our TDSE-calculated KER spectra with the vibrational energies in the light-induced upper Floquet potential curve relative to the dissociation limit for one-photon (1ω) dissociation $\varepsilon_{\text{diss}} = V_2(R \rightarrow \infty) - \omega$,

$$\varepsilon_v^{\text{KER}}(E_0, \theta) = \varepsilon_v^{\text{LIP}}(E_0, \theta) - \varepsilon_{\text{diss}}. \quad (4)$$

Within this Floquet interpretation of the KER, we thus assume that part of the nuclear wave packet is first promoted into the upper Floquet curve at the peak of the probe-laser pulse and dissociates along $V_{\text{upper}}^{\text{LIP}}$ to emerge after the passage of the probe pulse in the field-free O_2^+ ($f^4\Pi_g$) potential at large internuclear distances. Since LIPs are strongly dependent on the pulse intensity and temporal profile, this allows us to identify possible dynamical effects due to the transient trapping of the nuclear wave packet.

III. RESULTS AND DISCUSSION

In this section we characterize the imprints of LIPs in our quantum-mechanically calculated KER spectra for four representative probe-laser peak intensities I_0 between 10^{13} and 10^{14} W/cm^2 . We define the KER as the asymptotic kinetic energy of a single fragment (either O or O^+) and focus our discussion on fragments released with kinetic energies below 0.5 eV,

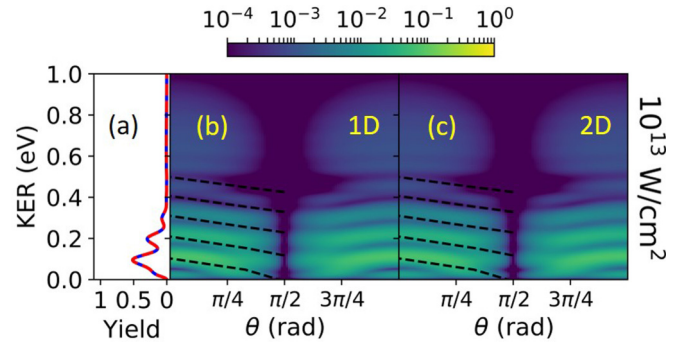


FIG. 2. (a) Total angle-integrated KER spectra for a 40-fs probe-laser pulse with a peak intensity of 10^{13} W/cm^2 . TDSE calculations without (1D) and including rotational excitations (2D) are represented by red dashed and blue solid curves, respectively. Corresponding angle-resolved KER spectra are shown for (b) 1D and (c) 2D TDSE calculations. Superimposed black dashed lines show the lowest five vibrational levels in the light-induced Floquet bond-hardening well according to Eq. (4). All spectra are normalized to the respective maximal fragment yields in Fig. 3(c).

which are primarily attributed to the 1ω dissociation process [2]. In the following sections, we investigate angle-integrated and angle-resolved KER spectra as well as fragment angular distributions for different probe-pulse peak intensities.

A. Signatures of transient nuclear-probability trapping in light-induced bond-hardening wells

In Fig. 2(a) we present the total angle-integrated KER spectra for the lowest peak intensity considered, 10^{13} W/cm^2 . At this intensity, our 1D and 2D calculations are indistinguishable, indicating that rotational excitations in the probe pulse are irrelevant. The energy spacing between the KER peaks of about 0.1 eV is in good agreement with the vibrational-level spacing in the field-free O_2^+ ($a^4\Pi_u$) state, as demonstrated in previous experimental and numerical investigations [9,10,23,38]. For better comparison, the fragment yields in the respective KER spectra in Fig. 2 and in Figs. 3(a)–3(c) are shown on the same scale and normalized to the maximal yields at the highest probe-pulse intensity 10^{14} W/cm^2 in Fig. 3(c).

In addition to the total KER spectra, we provide the corresponding angle-resolved KER spectra in Figs. 2(b) and 2(c). Except for minor differences near $\theta = \pi/2$, the results from 1D and 2D calculations are almost indistinguishable, again indicating that rotational excitation is not relevant. The angle-resolved KER spectra reveal striking fringe structures that shift downward in energy for increasing alignment angles $0 \leq \theta \leq \pi/2$. To analyze this downward trend, we compare our TDSE results with the Floquet light-induced vibrational energies given by Eq. (4) and indicated as superimposed black dashed curves in Figs. 2(b) and 2(c). The angular dependence of the fringes in the TDSE-calculated KER spectra is qualitatively reproduced by the Floquet prediction. The fringe structure disappears if the molecular alignment is perpendicular to the probe-laser polarization (at $\theta = \pi/2$), consistent with the vanishing effective electric-field strength E_{eff} and disappearance of the bond-hardening well. Due to the $\cos \theta$

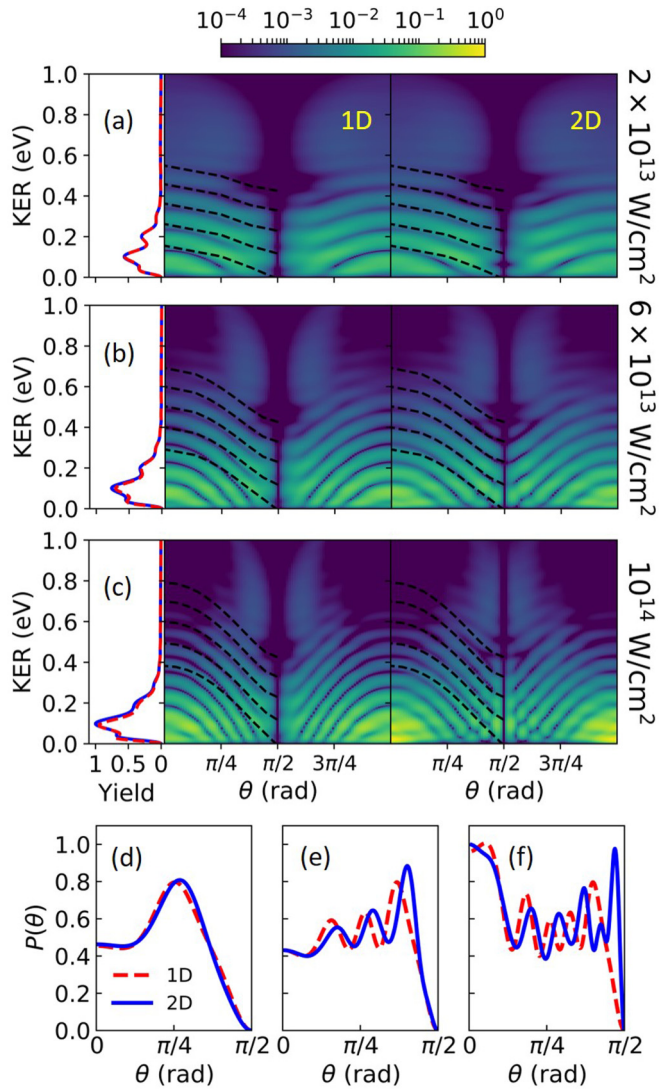


FIG. 3. Total angle-integrated (left column) and angle-resolved (middle and right columns) KER spectra for 40-fs probe-laser pulses with peak intensities of (a) 2×10^{13} , (b) 6×10^{13} , and (c) 10^{14} W/cm². All spectra are normalized to the respective maximal fragment yields in (c). The middle and right columns in (a)–(c) show results from TDSE calculations without (1D) and including rotational excitations (2D). Superimposed black dashed lines represent the five lowest vibrational levels in the light-induced Floquet bond-hardening wells according to Eq. (4). Fragment angular distributions $P(\theta)$ for the KER interval [0.2, 0.3] eV are shown in (d)–(f) for the same intensities as in (a)–(c), respectively, and normalized to the maximum in (f). Results from 1D and 2D TDSE calculations are represented by red dashed and blue solid curves, respectively.

dependence of E_{eff} , the gap between the lower and upper Floquet curves becomes narrower for angles closer to $\theta = \pi/2$. Thus, the angular dependence in E_{eff} translates into a downward shift of the vibrational spectrum in the upper Floquet curve, which appears to follow the energy shifts of the fringes in the KER spectrum. This suggests that the fringe structures in angle-resolved KER spectra contain information about the dissociation dynamics and the associated LIPs.

We next examine the validity of the Floquet interpretation of the fringe structures in angle-resolved KER spectra

for higher probe-pulse intensities. For this purpose, we show angle-integrated and angle-resolved KER spectra for probe-pulse peak intensities of 2×10^{13} , 6×10^{13} , and 10^{14} W/cm² in Figs. 3(a)–3(c), respectively. The TDSE-calculated angle-resolved KER spectra display intensity-dependent fringe structures that shift downward more rapidly for $0 \leq \theta \leq \pi/2$ as the peak intensity increases. These intensity-dependent shifts follow, in their overall trends, the Floquet vibrational energies obtained from Eq. (4) (shown as superimposed black dashed curves). As the probe-laser peak intensity is increased, the vibrational spectrum in the bond-hardening well of the associated upper LIPs shifts upward. Accordingly, at higher peak intensities, higher vibrational energies correspond to higher values of the predicted KER (except for $\theta = \pi/2$, where E_{eff} vanishes). This Floquet interpretation suggests that the intensity and angle-dependent fringe structures in the calculated KER provide an angle-dependent mapping of the underlying strong-field dissociation dynamics and associated LIPs. A closer inspection of Figs. 3(b) and 3(c) also shows that the fringes in the angle-resolved KER spectra appear at different positions for the 1D and 2D calculations. This difference between the 1D and 2D results increases with the probe-pulse peak intensity and is most pronounced close to $\theta = \pi/2$. This indicates the higher importance of rotational excitations for dissociation at angles near $\theta = \pi/2$ and for increasing peak intensity.

While the Floquet model qualitatively reproduces the angle and peak-intensity dependence of the angle-resolved fragment KER yields, noticeable differences remain in Figs. 3(a)–3(c). In particular, the angle-resolved KER spectra exhibit fringe structures at lower KER values than predicted by the Floquet model. In part, this mismatch is due to the Floquet interpretation behind Eq. (4) not taking the temporal variation of the LIPs into account, while in intense short laser pulses LIPs can vary significantly on the timescale of the nuclear motion. To quantify this comparison of timescales, we average over all alignment angles and track the motion of the nuclear wave packet in the bond-hardening well by following the expectation value of its internuclear distance $\langle R \rangle(t)$. For the considered range of peak intensities, the TDSE calculations consistently show that $\langle R \rangle(t)$ reaches the position of the 1ω -resonant transition at $R_{1\omega} \approx 3.4$ a.u. about 20 fs after the peak of the probe-pulse envelope. This travel time is comparable to the time it takes the probe-pulse electric-field envelope to drop to 50% of the peak probe-pulse field strength. The comparable timescales for the nuclear wave-packet motion and variation of the LIPs thus limit the applicability of the adiabatic Floquet model for quantitative predictions. By averaging over the temporal probe-pulse profile and calculating adiabatic Floquet LIPs for the reduced effective field strength $E'_{\text{eff}} = E_{\text{ave}} \cos \theta$, instead of E_{eff} , with the electric-field-strength (mean-square) average $E_{\text{ave}} < E_0$, the agreement at lower KER values can be improved.

B. Rotational dynamics near the LICI

By comparing KER spectra provided by our 1D and 2D calculations, we identify two main effects that are associated with rotational excitations: (i) dynamical alignment and (ii) rotational motion near the LICI. The first effect (dynamical alignment) is due to the torque which rotates initially

unaligned molecular ions toward the direction of the laser polarization [39–41]. This implies that dynamical alignment is responsible for the enhancement of the dissociation yield for aligned molecular ions ($\theta = 0$), as we have previously reported [3].

The second effect, the rotation of molecular ions toward the location of the LICI, can be identified in Figs. 3(b) and 3(c) as the increased low-KER fragment yield at alignment angles near $\theta = \pi/2$ predicted by the 2D calculation relative to the 1D results. It is consistent with the shape of the upper Floquet LIP near the LICI at the internuclear distance $R = R_{1\omega}$ and $\theta = \pi/2$ [cf. Fig. 1(a)]. For increasing probe-pulse peak intensity, the cone centered at the LICI becomes steeper. The larger potential gradient in turn leads to a stronger torque and thus to a more prominent role of the LICI in the dissociation dynamics at higher pulse intensities. This effect is demonstrated in Figs. 3(b) and 3(c) by the KER fringes near $\theta = \pi/2$ in the 2D results being shifted relative to their positions predicted by the 1D calculations. We furthermore notice the beadlike structures within the KER fringes near $\theta = \pi/2$ in the 2D calculation in Fig. 3(c). These structures do not occur in the 1D result, since it does not include rotational excitation and thus cannot correctly account for the nuclear dynamics near the LICI. These observations confirm that the rovibrational nuclear dynamics near the LICI gives rise to pertinent angle-dependent features in the angle-resolved KER spectra close to $\theta = \pi/2$.

Previous theoretical studies have attributed modulations in the angular distributions of photofragments to the dynamics at the vicinity of the LICI [33,34,42]. Experimentally, the appearance of such modulations in energy- and angle-resolved fragment distributions have been confirmed for the strong-field dissociation of H_2^+ molecular ions [35]. For O_2^+ , the present work allows the distinction between features that are due to the bond-hardening mechanism and those related to the dynamics near the LICI, based on the comparison between 1D and 2D calculations. So far, our results have shown that the angle-dependent fringe structures in the calculated angle-resolved KER spectra also emerge from 1D calculations that exclude rotational excitation. This means that the dynamics near the LICI is not responsible for the angle-dependent fringe structures in Figs. 2 and 3. Instead, as discussed in Sec. III A, these fringes extend over almost the entire range of dissociation angles and originate from the *transient trapping* of the nuclear probability density.

Figures 3(d)–3(f) show the normalized fragment angular distributions, obtained by integrating the respective yields in Figs. 3(a)–3(c) over a narrow KER interval between 0.2 and 0.3 eV. The angular distributions have pronounced modulations predicted by both 1D and 2D calculations, which reflect the fringe structures present in the angle-resolved KER spec-

tra. The frequency of these modulations varies drastically over the range of the considered peak intensities, indicating their overall sensitivity to the associated LIPs. The angle-dependent fringes predicted by the 2D calculations in Figs. 3(d)–3(f) are systematically shifted toward larger angles compared to the 1D results. These shifts are attributed to rotational motion toward the LICI and become more prominent for higher peak intensities. While we primarily attribute the intensity dependence of the angular distribution to transient trapping of the vibrational nuclear motion, we expect the diffraction effects in the nuclear dynamics near the LICI recently found by Natan *et al.* [35] in the dissociation of H_2^+ to also contribute to the specific angle-dependent behavior of the fragment distribution at larger angles $\theta \leq \pi/2$ in the dissociation of O_2^+ molecular ions.

IV. SUMMARY

We numerically solved the coupled-channel TDSE for the vibrational and rotational dynamics of O_2^+ molecular ions interacting with intense, short IR-probe laser pulses. Within the BO approximation, we restricted the bound and dissociative dynamics to the two relevant electronic states $\text{O}_2^+(a^4\Pi_u)$ and $\text{O}_2^+(f^4\Pi_g)$. We examined the possible signatures of the transient trapping of the nuclear wave packet and the associated LIPs in observable angle-resolved KER spectra. Our calculated angle-resolved KER spectra reveal distinct fringe structures that shift downward in energy as the alignment angle increases from $\theta = 0$ to $\pi/2$. In order to explain the underlying mechanism behind these shifting fringe structures, we compared our TDSE results with an adiabatic Floquet description of the dissociation dynamics based on the vibrational energies in the associated Floquet LIPs. For the range of probe-pulse peak intensities considered, 10^{13} – 10^{14} W/cm², the overall trends of the fringe structures in the quantum-mechanically calculated angle-resolved KER spectra are well reproduced by the proposed Floquet model. Moreover, our analysis shows that pertinent KER fringe structures close to $\theta = \pi/2$ are attributed to the field-driven rotational dynamics near the LICI.

ACKNOWLEDGMENTS

This work was supported by the Chemical Sciences, Geosciences, and Biosciences Division, Office of Basic Energy Sciences, Office of Science, U.S. Department of Energy under Award No. DEFG02-86ER13491. For part of the code development and for computational hardware, U.T. acknowledges support by NSF Grant No. PHY 1802085. We also acknowledge access to the Beocat Research Cluster at Kansas State University.

- [1] P. Cörlin, A. Fischer, M. Schönwald, A. Sperl, T. Mizuno, U. Thumm, T. Pfeifer, and R. Moshhammer, *Phys. Rev. A* **91**, 043415 (2015).
 [2] Y. Malakar, F. Wilhelm, D. Trabert, P. Kanaka Raju, X. Li, W. L. Pearson, W. Cao, B. Kaderiya, I. Ben-Itzhak, and A. Rudenko, *Phys. Rev. A* **98**, 013418 (2018).

- [3] P. M. Abanador, T. Pauly, and U. Thumm, *Phys. Rev. A* **101**, 043410 (2020).
 [4] A. S. Alnaser, B. Ulrich, X. M. Tong, I. V. Litvinyuk, C. M. Maharjan, P. Ranitovic, T. Osipov, R. Ali, S. Ghimire, Z. Chang, C. D. Lin, and C. L. Cocke, *Phys. Rev. A* **72**, 030702(R) (2005).

- [5] T. Ergler, A. Rudenko, B. Feuerstein, K. Zrost, C. D. Schröter, R. Moshhammer, and J. Ullrich, *Phys. Rev. Lett.* **97**, 193001 (2006).
- [6] B. Fischer, M. Kremer, T. Pfeifer, B. Feuerstein, V. Sharma, U. Thumm, C. D. Schröter, R. Moshhammer, and J. Ullrich, *Phys. Rev. Lett.* **105**, 223001 (2010).
- [7] U. Thumm, T. Niederhausen, and B. Feuerstein, *Phys. Rev. A* **77**, 063401 (2008).
- [8] M. Magrakvelidze, A. Kramer, K. Bartschat, and U. Thumm, *J. Phys. B* **47**, 124003 (2014).
- [9] M. Magrakvelidze, C. M. Aikens, and U. Thumm, *Phys. Rev. A* **86**, 023402 (2012).
- [10] S. Xue, H. Du, B. Hu, C. D. Lin, and A.-T. Le, *Phys. Rev. A* **97**, 043409 (2018).
- [11] F. Anis and B. D. Esry, *Phys. Rev. A* **77**, 033416 (2008).
- [12] M. Winter, R. Schmidt, and U. Thumm, *Phys. Rev. A* **80**, 031401(R) (2009).
- [13] M. Winter, R. Schmidt, and U. Thumm, *New J. Phys.* **12**, 023020 (2010).
- [14] B. Feuerstein, T. Ergler, A. Rudenko, K. Zrost, C. D. Schröter, R. Moshhammer, J. Ullrich, T. Niederhausen, and U. Thumm, *Phys. Rev. Lett.* **99**, 153002 (2007).
- [15] T. Seideman, M. Y. Ivanov, and P. B. Corkum, *Phys. Rev. Lett.* **75**, 2819 (1995).
- [16] S. Chelkowski, A. Conjusteau, T. Zuo, and A. D. Bandrauk, *Phys. Rev. A* **54**, 3235 (1996).
- [17] B. Feuerstein and U. Thumm, *Phys. Rev. A* **67**, 063408 (2003).
- [18] P. H. Bucksbaum, A. Zavriyev, H. G. Muller, and D. W. Schumacher, *Phys. Rev. Lett.* **64**, 1883 (1990).
- [19] G. Yao and S.-I. Chu, *Phys. Rev. A* **48**, 485 (1993).
- [20] L. J. Frasinski, J. H. Posthumus, J. Plumridge, K. Codling, P. F. Taday, and A. J. Langley, *Phys. Rev. Lett.* **83**, 3625 (1999).
- [21] M. Magrakvelidze, F. He, T. Niederhausen, I. V. Litvinyuk, and U. Thumm, *Phys. Rev. A* **79**, 033410 (2009).
- [22] I. A. Bocharova, A. S. Alnaser, U. Thumm, T. Niederhausen, D. Ray, C. L. Cocke, and I. V. Litvinyuk, *Phys. Rev. A* **83**, 013417 (2011).
- [23] S. De, M. Magrakvelidze, I. A. Bocharova, D. Ray, W. Cao, I. Znakovskaya, H. Li, Z. Wang, G. Laurent, U. Thumm *et al.*, *Phys. Rev. A* **84**, 043410 (2011).
- [24] M. Magrakvelidze, O. Herrwerth, Y. H. Jiang, A. Rudenko, M. Kurka, L. Foucar, K. U. Kühnel, M. Kübel, N. G. Johnson, C. D. Schröter *et al.*, *Phys. Rev. A* **86**, 013415 (2012).
- [25] J. Wu, M. Magrakvelidze, A. Vredenburg, L. P. H. Schmidt, T. Jahnke, A. Czasch, R. Dörner, and U. Thumm, *Phys. Rev. Lett.* **110**, 033005 (2013).
- [26] M. Magrakvelidze and U. Thumm, *Phys. Rev. A* **88**, 013413 (2013).
- [27] N. Saito, H. Sannohe, N. Ishii, T. Kanai, N. Kosugi, Y. Wu, A. Chew, S. Han, Z. Chang, and J. Itatani, *Optica* **6**, 1542 (2019).
- [28] A. Zavriyev, P. H. Bucksbaum, J. Squier, and F. Saline, *Phys. Rev. Lett.* **70**, 1077 (1993).
- [29] C.-C. Shu, K.-J. Yuan, D. Dong, I. R. Petersen, and A. D. Bandrauk, *J. Phys. Chem. Lett.* **8**, 1 (2017).
- [30] H. Ibrahim, C. Lefebvre, A. D. Bandrauk, A. Staudte, and F. Légaré, *J. Phys. B* **51**, 042002 (2018).
- [31] E. E. Aubanel, A. Conjusteau, and A. D. Bandrauk, *Phys. Rev. A* **48**, R4011 (1993).
- [32] S.-I. Chu and D. A. Telnov, *Phys. Rep.* **390**, 1 (2004).
- [33] G. J. Halász, Á. Vibók, N. Moiseyev, and L. S. Cederbaum, *Phys. Rev. A* **88**, 043413 (2013).
- [34] G. J. Halász, Á. Vibók, and L. S. Cederbaum, *J. Phys. Chem. Lett.* **6**, 348 (2015).
- [35] A. Natan, M. R. Ware, V. S. Prabhudesai, U. Lev, B. D. Bruner, O. Heber, and P. H. Bucksbaum, *Phys. Rev. Lett.* **116**, 143004 (2016).
- [36] A. Giusti-Suzor and F. H. Mies, *Phys. Rev. Lett.* **68**, 3869 (1992).
- [37] A. Giusti-Suzor, F. H. Mies, L. F. DiMauro, E. Charron, and B. Yang, *J. Phys. B* **28**, 309 (1995).
- [38] M. Zohrabi, J. McKenna, B. Gaire, N. G. Johnson, K. D. Carnes, S. De, I. A. Bocharova, M. Magrakvelidze, D. Ray, I. V. Litvinyuk *et al.*, *Phys. Rev. A* **83**, 053405 (2011).
- [39] J. H. Posthumus, J. Plumridge, M. K. Thomas, K. Codling, L. J. Frasinski, A. J. Langley, and P. F. Taday, *J. Phys. B* **31**, L553 (1998).
- [40] J. McKenna, A. M. Sayler, F. Anis, B. Gaire, N. G. Johnson, E. Parke, J. J. Hua, H. Mashiko, C. M. Nakamura, E. Moon *et al.*, *Phys. Rev. Lett.* **100**, 133001 (2008).
- [41] J. McKenna, F. Anis, A. M. Sayler, B. Gaire, N. G. Johnson, E. Parke, K. D. Carnes, B. D. Esry, and I. Ben-Itzhak, *Phys. Rev. A* **85**, 023405 (2012).
- [42] A. Tóth, A. Csehi, G. J. Halász, and A. Vibók, *Phys. Rev. A* **99**, 043424 (2019).